Device physics of colloidal quantum dot solar cells

Speirs, Mark Jonathan

3 PbS-CdS core-shell quantum dot solar cells

Abstract

The high surface to volume ratio of lead sulfide quantum dots (PbS QDs) leads to a high density of detrimental trap states caused by lattice imperfections on the QD surface. Introducing a thin shell of a wide bandgap semiconductor to the QD surface is a promising method to passivate these trap states. Here we demonstrate solar cells made from PbS-CdS core-shell QDs, yielding a 147 mV increase in V_{OC} compared to core-only PbS QDs. We explore the physical reason for this enhancement and demonstrate that it is indeed caused by improved passivation of the PbS surface by the CdS shell, leading to a lower electron trap density.

Published as:

M. J. Speirs, D. M. Balazs, H.-H. Fang, L.-H. Lai, L. Protesescu, M. V. Kovalenko and M. A. Loi, *J. Mater. Chem. A* **2015**, 3, 1450-1457

3.1 Introduction

After synthesis, lead chalcogenide QDs are typically surrounded by long aliphatic ligands such as oleic acid (OA) or oleylamine. The ligands provide solubility in apolar solvents, prevent ripening or aggregation, and passivate the particle surface. These ligands, however, also act as a barrier to charge transfer and transport between neighboring QDs, and must therefore be removed for electronic device applications. Typically, this is done by exposing the QD film to one or more shorter ligands, such as aromatic thiols,[1,2] short alkyl thiols,[3,4] mercaptopropionic acid,[5] and more recently, halide anions.[6,7] When ligand exchange takes place, the inter-dot distance is decreased, and the electronic wave functions between adjacent QDs overlap. This allows charge carrier mobilities in the QD film to be enhanced by several orders of magnitude.[8]

Nevertheless, the ligand-exchange procedure also introduces many surface defects such as vacancies and dangling bonds.[9] These defects favor trap-assisted recombination, which inhibits the splitting of the quasi-Fermi energy levels under illumination and consequently limits the maximum achievable open circuit voltage (V_{OC}).[4,10,11] For this reason, proper electronic passivation of ligand-treated QD surfaces is a crucial prerequisite for highly efficient solar cells. One method to passivate the QD surface focuses on repairing surface defects by post-deposition exposure of QD films to various small molecular and atomic ligands.[7,12] Another, less explored, method is to introduce a passivation layer already during the synthesis of the QD in order to prevent trap states rather than repair them. The latter strategy can be achieved by introducing a shell of a wide bandgap semiconductor such as CdS to the surface of PbS, thus obtaining obtain PbS-CdS core-shell QDs.

Recently, we reported PbS-CdS core-shell QD sensitized solar cells on mesoporous TiO_2 nanoparticles, using 3-mercaptopropionic acid ligand exchange.[13] A substantial increase in V_{OC} of 150 mV was observed when covering PbS QDs with a 0.5 nm thick shell of CdS. Further increasing the shell thickness provided only a marginal additional increase in V_{OC} and was accompanied by a significant drop in J_{SC} due to the added barrier for charge transport. It was also shown that the mean electron lifetime and diffusion length increases with increasing shell thickness, suggesting that the increase in V_{OC} is due to suppressed non-radiative charge recombination. Other reports have also described PbS-CdS QDs in solar cells,[14] most recently exhibiting

a power conversion efficiency (*PCE*) of 5.6% with PEDOT and ZnO as hole and electron transporting layers, respectively.[15] Also in this case, the device improvement is due to an increased V_{OC}, and the best results are obtained for very thin shell thicknesses (~0.1 nm). So far, the increase in V_{OC} has been attributed solely to increased surface passivation, but before this can be concluded, one must take care to exclude differences in energy levels between the two systems (core-only and core-shell QDs) as the origin of the improvement of V_{OC}. In a previous work, the bandgaps of the OA-capped QDs were compared in solution.[15] However, the bandgap and energy levels depend on the capping ligands,[16] and these effects may be different for core-only and core-shell QDs. Therefore, for accurate cross-comparison, the bandgap must be compared in the ligand-treated film rather than in solution.[17] Furthermore, the position of the Fermi level has an important role in determining the V_{OC} since it affects the degree of band bending within the active layer.

The purpose of this chapter is therefore to explain in detail the physical origin of the increased V_{OC}. To probe the properties of the material itself, the simplest solar cell architecture, the metal/QD Schottky device, is investigated. In this architecture, core-shell QDs exhibit a V_{OC} = 0.59 V, which is 147 mV higher than the core-only reference device. The origin of the increased V_{OC} is explained using impedance spectroscopy, time-resolved photoluminescence spectroscopy, light intensity dependent V_{OC} measurements, and bottom-gated field effect transistors (FETs). All investigations point to the reduction of traps on the QD surface as the main origin of the increased V_{OC}.

3.2 Results and discussion

3.2.1 Quantum dot characterisation

PbS QDs are synthesized using a previously described hot-injection method.[13] Core-shell QDs are then obtained by Cd^{2+} cation exchange in parent PbS QDs.[18] After the shell is formed, a blueshift of the first excitonic peak from 1095 nm to 1069 nm is observed (Figure 3.1b), which is attributed to the size reduction of the PbS core when Pb^{2+} atoms are replaced by Cd^{2+}. The size of the PbS QDs is determined to be 3.69 nm using an empirical formula developed by Moreels et al. relating the bandgap E_g and the diameter d of PbS

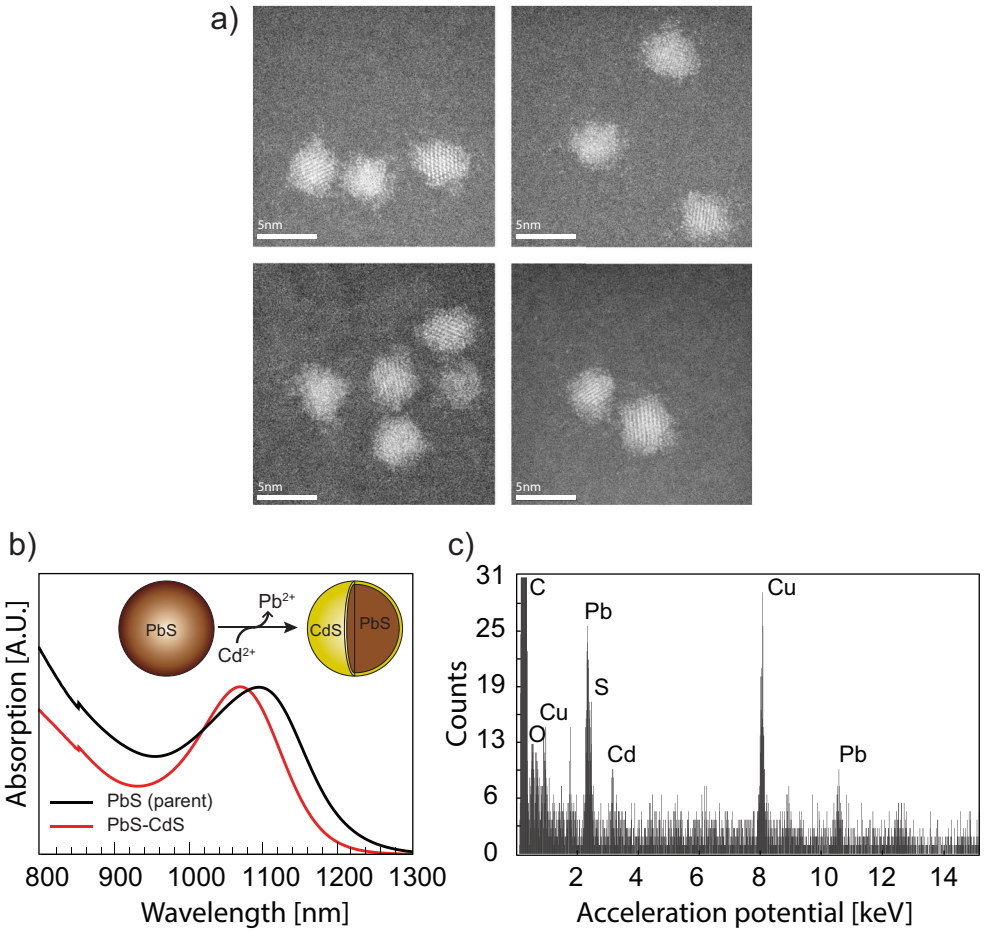

Figure 3.1. a) Scanning transmission electron microscope (STEM) micrographs of the OA-capped core-shell QDs. b) Absorption spectra of the core-only QDs used prior to Cd2+ cation exchange (black) and the resulting core-shell QDs (red) after cation exchange. The inset shows a schematic of the cation exchange process b) Energy-dispersive X-ray spectroscopy (EDXS) measurement of the core-shell QDs. The atomic labels have been added to the peaks of interest, in particular to indicate the presence of Cd atoms in the shell.

QDs in nanometres,[19]

$$E_g\,[eV] = 0.41 + \frac{1}{0.0252d^2 + 0.283d}. \tag{3.1}$$

From the blueshifted peak of the core-shell QDs, this equation indicates a reduced core diameter of 3.57 nm and, consequently, an approximated shell

thickness of 0.065 nm. The actual shell thickness is likely higher, since this equation assumes perfectly spherical particles and does not take into account the shared sulfur atom between the Pb and Cd atoms. Furthermore, the shell allows partial relaxation of quantum confinement of the charge carrier wavefunctions into the shell compared to the ligand/solvent environment, leading to a partial reduction of the blueshift and an underestimation of the shell thickness. The overall diameter of the core-shell QDs observed in scanning TEM (STEM) micrographs is the same as the parent core diameter within measurement resolution. Although the similar lattice parameters of PbS (rock salt, a = 0.59 nm) and CdS (zinc blende a = 0.58nm) impede direct observation of the shell in the micrographs, the presence of the CdS shell is confirmed by energy-dispersive X-ray spectroscopy (EDXS) measurements performed on the QDs shown in Figure 3.1b.

Ligand exchange has been demonstrated to be a fundamental step towards increasing QD film conductivity.[20] In this chapter, ligand exchange is achieved by exposing QD films to a solution of 1,4-benzenedithiol (BDT) in acetonitrile, and the optical bandgap is examined both before and after ligand exchange. For the core-only QDs the ligand exchange process results in a significant redshift of the excitonic peak from 1023 nm to 1048 nm in the absorbance spectrum (Figure 3.2a). This is explained by partial loss of quan-

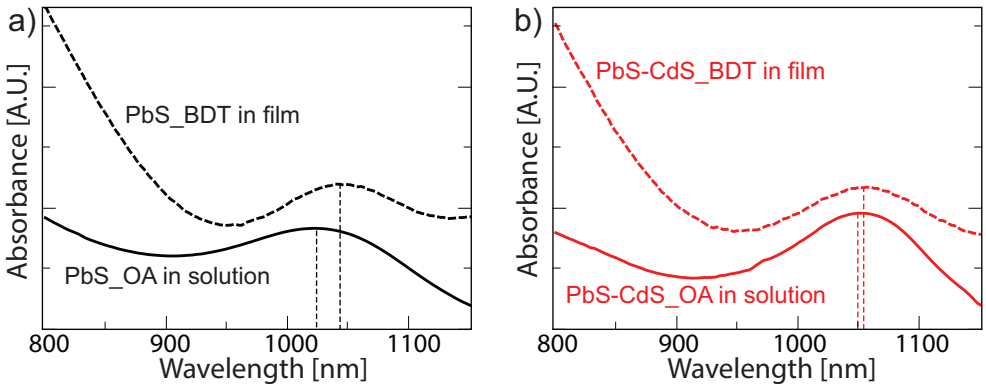

Figure 3.2. Absorbance spectra of OA-capped QDs in solution (solid line) and capped with BDT in film (dashed line) for a) core-only QDs and b) core-shell QDs.

tum confinement when the inter-dot distance is decreased . In contrast, the core-shell QDs undergo a much smaller redshift upon ligand exchange (Figure 3.2b), indicating that quantum confinement is much more preserved, due to the additional barrier caused by the CdS shell. The distance between BDT-

treated PbS QDs has previously been shown to be ~0.5 nm.[9] The addition of a 0.1 nm shell to each QD effectively increases the distance between the cores by ~40%, which affects the degree of wave function overlap between adjacent QDs, and consequently the bandgap. Recently, we have developed a method to determine the electronic bandgap of this class of materials using ionic liquid gated field effect transistors.[17] For these materials, the electronic bandgap obtained with this method differs only 2-5% with the optical bandgap. In this thesis therefore, the position of the excitonic peak is used for facile determination of the optical and electronic bandgap. Both types of QDs used in this chapter exhibit excitonic peaks around 1050 nm in film, corresponding to a bandgap of 1.18 eV.

3.2.2 Core-shell quantum dot solar cells

PbS and PbS-CdS Schottky solar cells with active layer thickness of ~130 nm are fabricated in inert atmosphere using the previously mentioned layer-by-layer deposition procedure.[1,21] The resulting *J-V* responses of these devices are shown in Figure 3.3, and the device figures of merit are summarized in Table 3.1.

Table 3.1. Summary of solar cell figures of merit. The average values and standard deviation are given in brackets.

Device	V_{OC} [V]	J_{SC} [mA/cm^2]	FF [%]	*PCE* [%]
PbS	0.44 (0.44±0.02)	10.8 (9.3±1.3)	43 (42±2)	2.1 (1.7±0.3)
PbS-CdS	0.59 (0.42±0.06)	10.0 (8.2±1.5)	44 (45±5)	2.5 (2.0±0.5)

For the core-only devices, a V_{OC} of 0.44 V, a J_{SC} of 10.8 mA cm 2, a FF of 43%, and a *PCE* of 2.1% are observed. It should be noted that while the J_{SC} and *FF* in these devices are lower than in our previous reports, the V_{OC} is comparable to that of the best Schottky devices reported for PbS QDs of similar bandgap.2 For the best core-shell device, a slightly smaller J_{SC} of 10.0 mA/cm^2, a largely unchanged *FF* of 44%, and a significantly increased V_{OC} of 0.59 V are observed, resulting in a *PCE* of 2.5%. This increase in V_{OC} is comparable to what has been recently reported for core-shell QDs.[15,22] A

significantly reduced loss of V_{OC} is observed compared to the built in voltage V_{bi}, defined as the voltage where the light and dark current are equal; the difference between the V_{OC} and V_{bi} for the core-only device is 62 mV, while for the core-shell device the difference is only 2 mV. A histogram of the V_{OC}s for all prepared devices is displayed in the Figure 3.3c, showing the high level of reproducibility of the V_{OC} improvement.

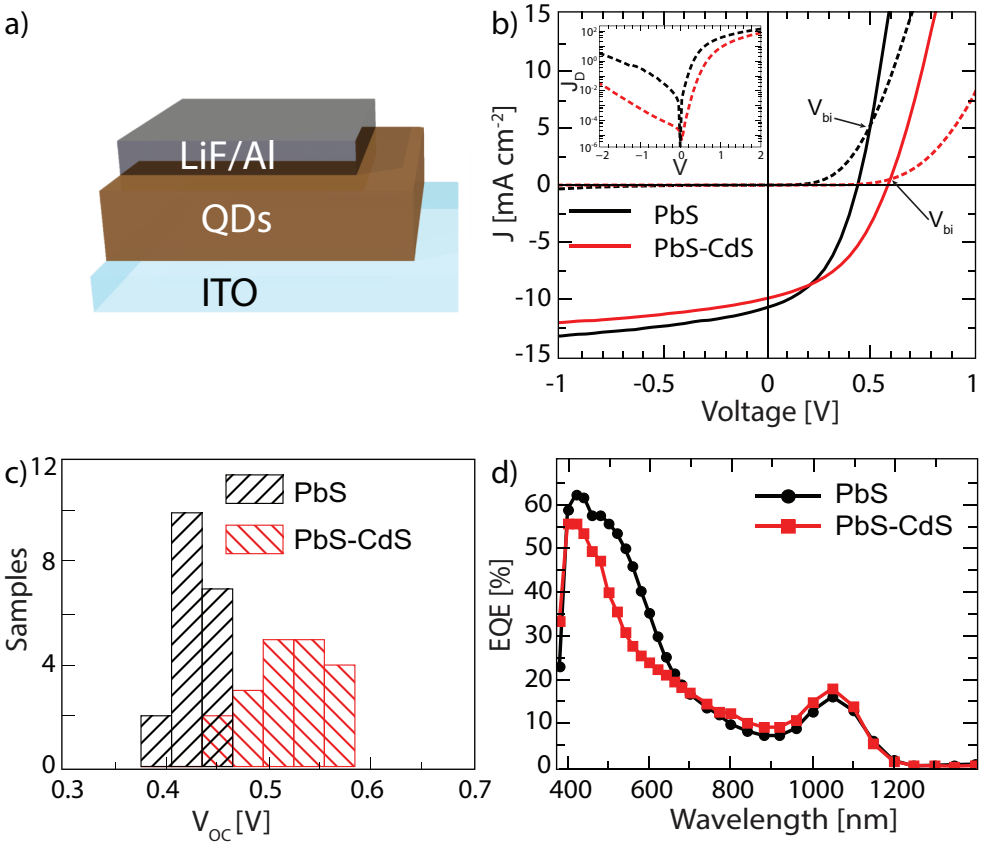

Figure 3.3. a) Schottky device structure b) *J-V* characteristics in the dark (dashed lines) and under AM1.5G illumination (solid lines) for Schottky devices fabricated with PbS QDs (black) and PbS-CdS QDs (red). b) Schottky device structure. c) Histogram of the V_{OC}s for all devices made. d) *EQE* spectra of the same devices.

3.2.3 Origin of the increased open circuit voltage

To understand if there is any difference in the Fermi energy level between core-only and core-shell QDs, impedance spectroscopy measurements of the Schottky devices are conducted in the dark under forward bias conditions. Devices as thin as ~70-80 nm are fabricated to ensure that the depletion width extends throughout the active layer. The impedance spectra for both the core-only and core-shell devices feature a single semicircular arc (Figure 3.4a-b, which is fitted using the equivalent circuit displayed in the inset to obtain the capacitance per unit area ($C' = C/A$, where A is the device area defined by the electrode overlap). From the Mott-Schottky equation we have,

$$\frac{1}{C'^2} = \left(\frac{2}{qN\varepsilon_r\varepsilon_0}\right)\left(V - V_{fb} - \frac{kT}{q}\right), \tag{3.2}$$

where N is the density of free charge carriers in the device, ε_r is the relative permittivity of the material, and ε_0 is the permittivity of vacuum. Thus, plotting C'^{-2} versus the applied bias allows the flat-band potential V_{fb} to be extracted as a qualitative measure of the depth of the Fermi level in the bandgap. For the core-only device we find $V_{fb} = 758$ mV, whilst for the core-shell we find a slightly lower value of 734 mV. Since the flat-band potential is an upper limit for the maximum obtainable open circuit voltage, the slightly lower value found in the core-shell QDs has a small detrimental effect on the value of the V_{OC}, and cannot explain the increased V_{OC} found in the experiments. From the slope of the Mott-Schottky curves, similar doping concentrations of $9.6 \cdot 10^{16}$ and $1.9 \cdot 10^{17}$ cm^{-3} were found for the core-only and core-shell respectively.

The geometric permittivity of these materials can be obtained from the capacitance of fully depleted devices. To avoid chemical contributions to the capacitance devices must be fabricated with thicknesses less than the depletion width $w = \left({}^{2\varepsilon_r\varepsilon_0}/_{eN} \cdot V_{bi}\right)^{1/2}$,[23] which equals 124 ± 5 nm and 76 ± 4 nm for core-only and core-shell QDs respectively. The capacitance of devices with thickness 70-80 nm are measured at zero bias, and the parrallel plate model is used to calculate the permittivity $C' = \varepsilon_r\varepsilon_0/d$, where d is the device thickness. Relative permittivities are calculated to be $\varepsilon_r = 21 - 24$ for core-only and $\varepsilon_r = 15 - 17$ for core-shell QDs. Despite this significant difference in permittivity, the electronic bandgap calculated from the excitonic peak is not greatly influenced, since for both QDs, the excitonic binding energies are

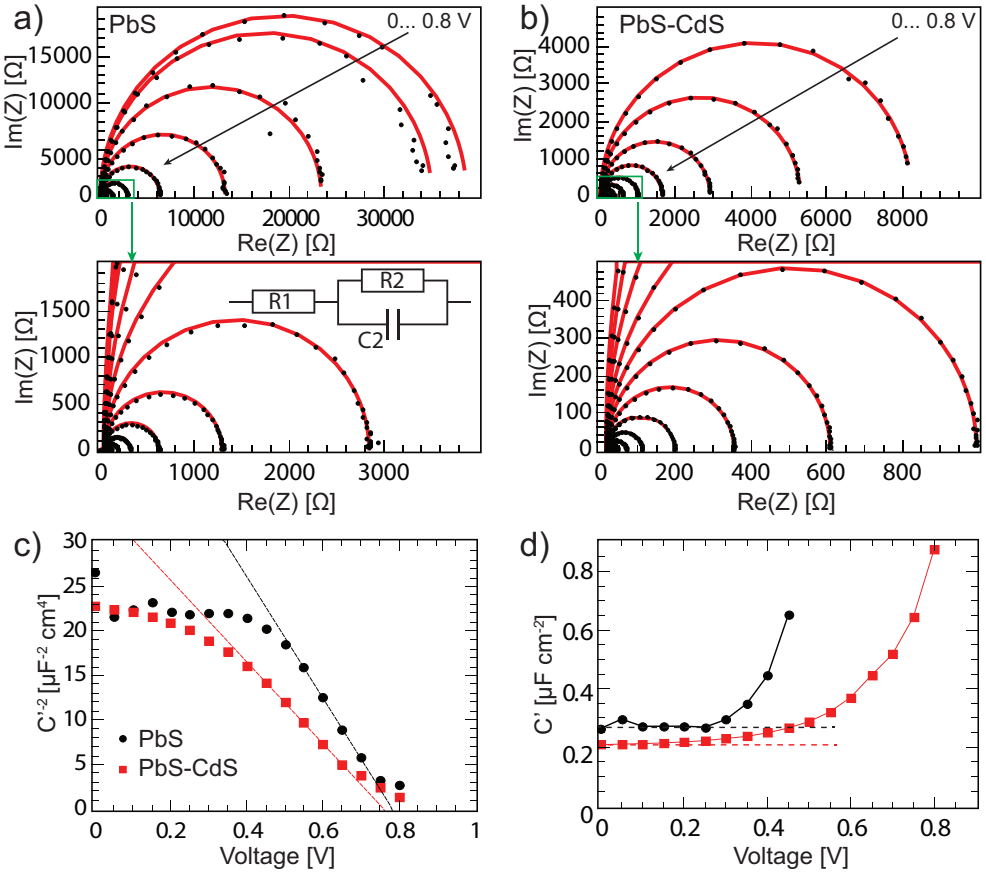

Figure 3.4. a) Nyquist plots for a) PbS only and b) PbS-CdS core-shell QDs. The black dots represent the data points while the red lines show the fits using the equivalent circuit displayed in the inset. Magnifications of the areas highlighted in green are given in the lower panels. c) Mott-Schottky plot of the capacitance extracted from a-b). The dotted lines are fitted to the linear regime. d) C' for core-only (black circles) and core-shell QDs (red squares).

very small.*

*We can calculate the excitonic binding energy E_b of a semiconductor using $E_b = \varepsilon^{-2} m_e m_h (m_e + m_h)^{-1} m^{-1} Ry$, where m_e and m_h are the effective electron and hole mass, m is the free electron mass, and Ry is Rydberg's constant. Assuming the effective mass of charge carriers in the core is not affected by the thin shell, we can use $m_e = m_h = 0.09m$,[24] to obtain $E_b = 1.2$ meV for PbS QDs and $E_b = 2.1$ meV for PbS-CdS QDs. This is negligible compared to the optical bandgap

Time resolved PL measurements can give important information on the dynamics of the photoexcitations in our QD films, and consequently on the formation of photoexcited carriers. From the transient measurements reported in Figure 3.5, the lifetimes of excited states are extracted both for OA and BDT-capped QDs. For the OA-capped QD films, the dynamics are described by mono-exponential decay with lifetime $\tau = 42$ ns for the core-only and a more than one order of magnitude higher lifetime of $\tau = 406$ ns for core-shell QDs, which is similar to the results found by Sanchez et al.[25] After ligand exchange with BDT, a reduction of the decay time of more than two orders of magnitude is observed for both types of QDs and the decay dynamics become bi-exponential, with a fast component $\tau_1 = 0.12$ ns and a slower component $\tau_2 = 0.98$ ns for core-only QDs, while the values $\tau_1 = 0.33$ ns and $\tau_2 = 4.2$ ns are found for core-shell QDs. Interestingly, the increased lifetime of the core-

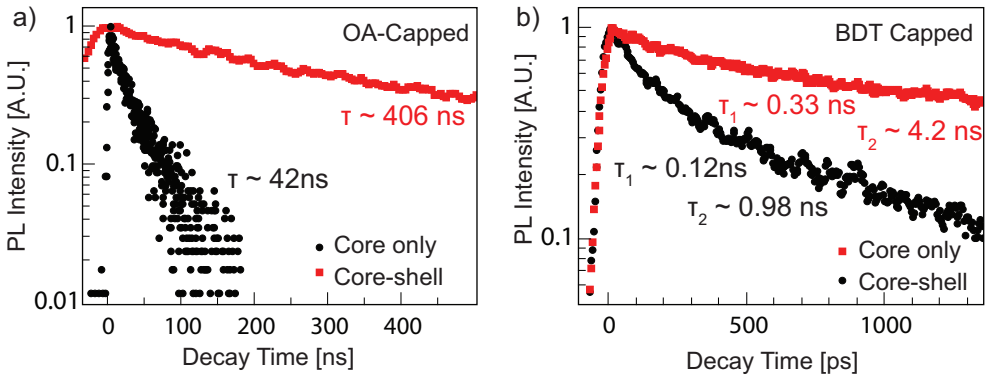

Figure 3.5. a) Photoluminescence decay dynamics of OA-capped QD films, and the corresponding time constants extracted by mono-exponential decay fitting. b) Photoluminescence decay dynamics for QD films after ligand exchange with BDT, and the corresponding time constants extracted from bi-exponential decay fitting.

shell QDs occurs despite a lower permittivity, which leads to reduced dielectric screening of the radiating field inside the QDs.[26] Although this increase may be at least partially due to improved surface passivation, other factors must also be considered. It has been shown for example, that for PbSe-CdSe core-shell QDs with shell thickness of 1.6 nm the charge carrier lifetime is increased due to a reduced electron-hole overlap within a single QD, caused by the de-localization of the electron wave-function into the shell while the hole is confined to the core.[27] Since the QDs used in this study have an extremely thin shell, this effect is assumed to be negligible. The quantum confinement

must also be considered as an important parameter affecting exciton lifetime, since in more confined systems the charge carriers have less probability for bimolecular recombination. We have seen from the absorption spectra that the degree of quantum confinement does differ significantly, therefore it is difficult to separate the effect of reduced trap-assisted recombination from the effect of reduced bimolecular recombination. The effect of surface passivation is expected to be more evident in the BDT-capped QDs, since many of the traps in PbS QDs are introduced during the ligand exchange process. The difference in lifetimes between the core-only and core-shell QDs, however, is larger for the OA-capped QDs, suggesting that quantum confinement is the dominant factor in these measurements, and not surface passivation.

The current density in an ideal Schottky solar cell can be described by the Schokley diode equation,

$$J = J_0 \left[exp\left(\frac{qV}{nkT}\right) - 1 \right] - J_{PH}, \tag{3.3}$$

where J_0 is the reverse saturation current density, J_{PH} is the photocurrent, n is the ideality factor, k is Boltzmann's constant, T is the temperature, and V is the applied voltage across the solar cell. The ideality factor is determined by the dominant trapping mechanism in the solar cell, and is therefore an informative parameter to determine the degree of surface passivation in these devices. One method to obtain the ideality factor is by fitting the exponential regime of the dark current J_D as a function of the applied bias. This method is complicated for the solar cells studied here due to the lack of a well-defined exponential regime at low forward bias (inset Figure 3.3b). Therefore the ideality factor is in this case more accurately determined at open circuit conditions ($J = 0$), for which Equation 3.3 can be rearranged to

$$V_{OC} = \frac{nkT}{q} \ln\left(\frac{J_{PH}}{J_0}\right) \tag{3.4a}$$

$$= \frac{nkT}{q} \alpha \ln(I) + c \tag{3.4b}$$

For the latter equality, we have made use of the relationship $J_{PH} \propto I^{\alpha}$, where I is the illumination intensity, α is an empirical parameter indicating the linearity of the photocurrent with intensity, and c is a fitting parameter collecting all the terms independent of light intensity. For these solar cells, α is found to be 0.96 and 1.00 for the core-only and core-shell QDs respectively, as shown in

Figure 3.6a. Hence, by plotting the V_{OC} against the illumination intensity I on a semi-logarithmic plot, the ideality factor n can be extracted from the slope of the curve. The ideality factor gives an indication of the dominant recombination mechanism in the device, with $n = 1$ corresponding to ideal bimolecular recombination, and $n = 2$ corresponding to fully trap-assisted recombination via mid-gap trap states.[10,28] Two regimes are observed for both the core-only and the core-shell QDs (Figure 3.6b). At low light intensity, when the ratio of traps to photo-generated charge carriers is relatively high, both devices are trap dominated, with $n = 2.04$ and $n = 1.93$ for the core-only and core-shell, respectively. As the light intensity is increased, more traps are filled and the density of charge carriers increases, increasing the probability of bimolecular over trap-assisted recombination. For the core-only QDs, this leads to a reduction of the ideality factor to $n = 1.46$, indicating that trap-assisted and bimolecular recombination both play a significant role at 1-Sun intensity. For the core-shell QDs at about 1-Sun intensity, we have $n = 1.08$, establishing that bimolecular recombination dominates in core-shell QDs under these conditions. Therefore, this validates the idea that trap-assisted recombination is suppressed in core-shell QDs.

One of the consequences of a high density of trap states is the pinning of the Fermi level to the trap energy levels. Therefore, the ability to shift the Fermi level within the bandgap via an applied bias gives insight into the density of trap states. For this reason, SiO_2-gated FETs were fabricated, of which

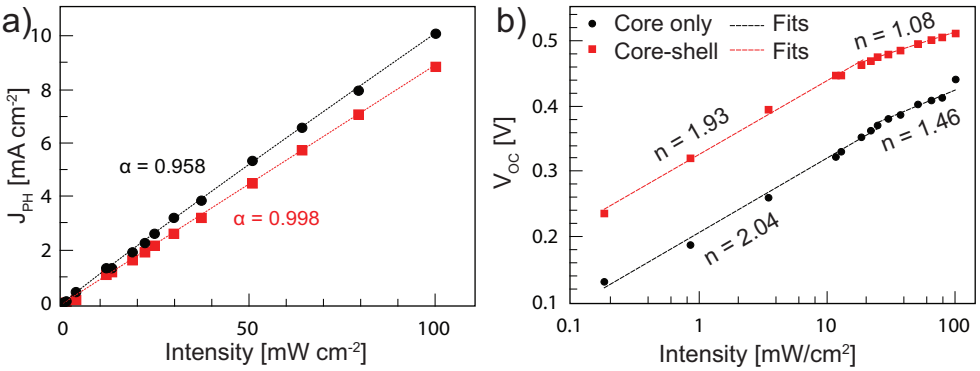

Figure 3.6. a) V_{OC} dependence on the illumination intensity I for core-only QDs (black circles) and core-shell QDs (red squares). The ideality factors are obtained by fitting the data with the equation $V = {}^{nkT}/_{q}\ln(I) + c$ b) Intensity dependence of the photocurrent at short circuit conditions for the core-only QDs (black circles) and core-shell QDs (red squares). The data are fitted with the equation $J(I) = cI^{\alpha}$.

the output and transfer characteristics are shown in Figure 3.7. Both the core-only and core-shell transistors exhibit ambipolar transport behaviour. The gating effect for the core-shell QDs is slightly larger for the p-channel (Figure 3.7a, left panel) and significantly enhanced for the n-channel compared to core-only QDs (Figure 3.7a, right panel). From the transfer characteristics of the n-channel (Figure 3.7b), a shift in the sub-threshold gate voltage and a decreased sub-threshold swing is observed from 9.1 V/dec for the core-only to 6.3 V/dec for the core-shell QD FETs. The improved gating effect and steeper sub-threshold swing in the n-channel indicate that the Fermi level can be moved more freely in the core-shell QDs, and is less pinned by trap states than

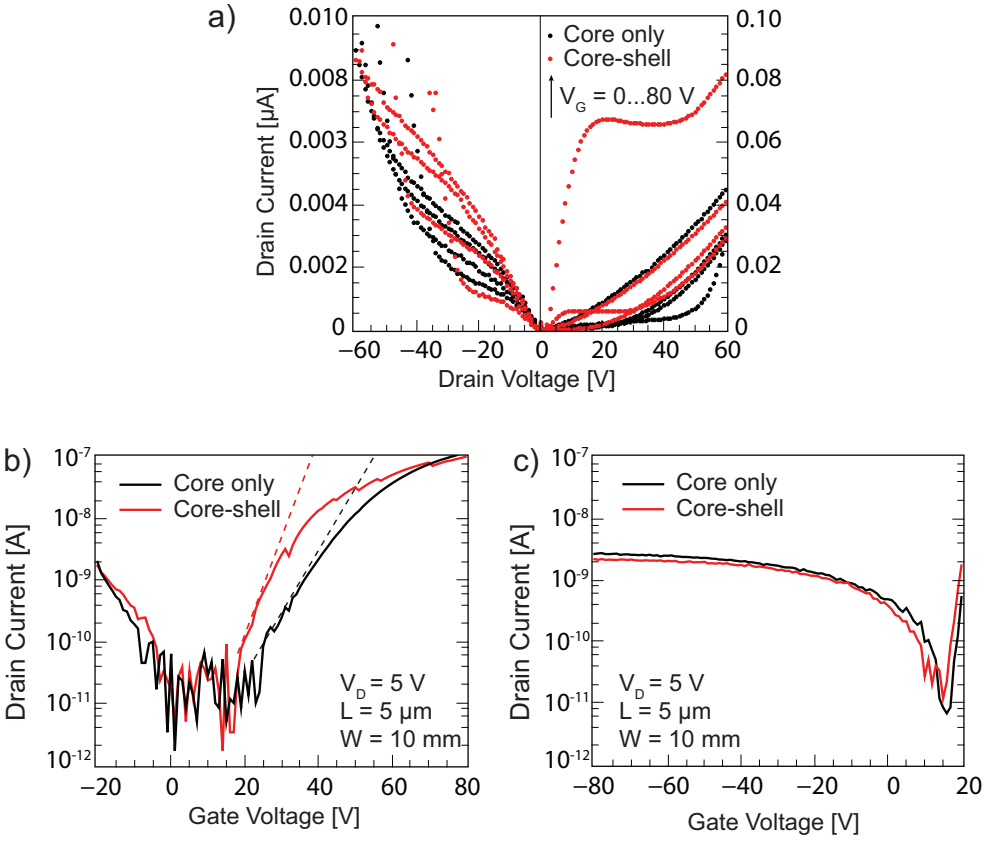

Figure 3.7. a) FET output characteristics for the core-only (black) and core-shell (red) QDs. Not the difference in scale between the right and left panels. b) n-channel transfer characteristics. The dotted lines are added to emphasize the increased sub-threshold swing for the core-shell QDs. c) p-channel transfer characteristics.

in the core-only QDs.[29] For the p-channel transfer characteristics, no significant change is observed between the two types of QDs (Figure 3.7c), suggesting that the CdS shell passivates mostly electron traps. Charge carrier mobility values are extracted from the linear current regime according to the gradual channel approximation and using a parallel plate capacitor model for the gate electrode charge accumulation. In this way, for the core-only QDs, charge carrier mobilities of $\mu_h = 5.9 \cdot 10^{-8}$ cm^2/Vs and $\mu_e = 5.5 \cdot 10^{-6}$ cm^2/Vs are obtained for the hole and electron respectively. For the core-shell QDs, a similar value for the hole mobility is found $\mu_h = 5.5 \cdot 10^{-8}$ cm^2/Vs and a marginally lower electron mobility $\mu_e = 4.1 \cdot 10^{-6}$ cm^2/Vs for the core-shell QDs.

3.3 Conclusion

We have demonstrated enhanced Schottky solar cells with PbS-CdS core-shell QDs. In comparison with core-only PbS QDs, devices fabricated with core-shell QDs give rise to an increase in the V_{OC} of up to 147 mV. We have excluded an altered bandgap as the origin of the improved V_{OC} by adjusting the QD counterparts to exhibit identical bandgaps after film formation and ligand exchange, and demonstrated an almost identical flat-band potential for both types of QDs to exclude the effect of a shifted Fermi level.

From absorbance spectra, a much smaller redshift for core-shell QDs is observed after ligand exchange, indicating increased quantum confinement, leading to a longer excitation lifetime as revealed by time resolved PL spectroscopy. The dominant recombination mechanism in core-shell QDs is determined to be trap-assisted recombination at low light intensity. At 1-Sun intensity, however, bimolecular recombination takes over for core-shell QDs, indicating an effective filling of the trap states. In contrast, core-only QDs maintain a signature of trap-assisted recombination even at 1-Sun intensity.

FETs fabricated with core-shell QDs demonstrated increased shifting of the Fermi level under applied gate voltage for the n-channel, demonstrating a reduced electron trap density. The reduced trap density allows more efficient splitting of the quasi-Fermi levels in core-shell QDs and consequently a higher V_{OC}, making this a highly promising material for QD solar cell applications.

3.4 Experimental Details

QD synthesis: PbS QDs are synthesized using a previously described hot injection method,[30] in which a lead precursor solution of 1.516 g $Pb(CH_3COO)_2 \cdot H_2O$ in 50 ml ODE and 4.5 ml OA is vacuum dried at 120 °C in a three-neck reaction flask. The temperature is subsequently raised to 145 °C after which a sulfur precursor of 0.420 ml bis(trimethylsilyl) sulfide in 10 ml 1-octadecene (ODE) is quickly injected and the flask cooled in a water bath. Hexane and ethanol are added to the solution, followed by centrifugation to separate the QDs. Two more washing steps are performed by re-dispersion in hexane and precipitation by ethanol and finally the QDs are re-dispersed in chloroform. PbS-CdS QDs are obtained by Cd cation exchange in PbS QDs, described in detail elsewhere.[31] In short, parent PbS QDs are injected into a three-neck flask containing a solution of CdO, ODE and OA, and kept at 100 °C for a reaction time of 45 minutes. Ethanol is then used to precipitate the PbS-CdS core-shell particles, after which two re-dispersion/precipitation steps are performed with toluene and ethanol respectively. Finally, the PbS-CdS core-shell particles are re-dispersed in chloroform.

STEM and EDXS characterization: STEM micrographs are made using a FEI Tecnai F30 microscope, operating at 300 kV acceleration potentail. EDXS analysis is performed using a JEOL JSM-6400 scanning electron microscope. Samples are fabricated by dropcasting 1-2 μL of 2.5 mg/ml solution of QDs in toluene onto a carbon coated copper grid. No further washing treatment is performed.

Solar cell fabrication: In inert atmosphere, PbS or PbS-CdS QDs are spin-casted from chloroform solution (10 mg/ml) on substrates pre-patterned with indium tin oxide (ITO). Ligand exchange is carried out by exposing the film to a 20 mM solution of BDT in acetonitrile for 30 seconds, followed by spin-drying without any additional washing steps. Complete removal of the OA ligand by this method has previously been confirmed by FTIR spectra.[1,21] This process is repeated ~10 times, yielding smooth films of approximately 130 nm thick as determined by a Dektak Profilometer. The devices are then annealed at 140 °C for 5 minutes. Sintering or major modification of the QD surface from this step can be ruled out by observing the unchanged excitonic peak from absorption measurements. Finally, the top contacs are deposited

by thermal evaporation of 1 nm LiF and 100 nm Al at < 10^{-6} mbar. Device areas are defined by the overlap of the Al and ITO electrodes to be 16 mm^2. In total, 19 devices were fabricated for each type of QD.

Transistor fabrication: Silicon substrates covered by a 230 nm thick SiO_2 layer and pre-patterned gold electrodes with 5 μm channel length and 10 μm channel width are used for transistor fabrication, upon which a ~50 nm film of QDs is deposited using the same layer-by-layer method and annealing step used for solar cell devices. The measurements are performed in inert atmosphere using an Agilent E5262A Semiconductor Parameter Analyzer.

J-V **characterization:** Current-voltage sweeps are carried out in inert atmosphere under simulated AM1.5G solar illumination using a Steuernagel Solarconstant 1200 metal halide lamp set to 100 mW/cm^2 intensity, as measured by a silicon reference cell, and corrected for the spectral mismatch.[32] Under illumination, a shadow mask with slightly smaller area (9 mm^2) is used to exclude lateral contributions to the photocurrent from beyond the device area.

***EQE* measurements:** External quantum efficiencies are measured under monochromatic light conditions at short circuit conditions, using the same shadow masks as in the *J-V* characterization measurements. As a light source, a 250 W quartz tungsten halogen lamp (6334NS, Newport) with lamp housing (67009, Newport) is used. Monochromatic light is achieved using narrow band pass filters (Thorlabs) with a full width half maximum (FWHM) of 10 $\pm$ 2 nm from 400 nm to 1300 nm and a FWHM of 12 $\pm$ 2.4 nm from 1300 nm to 1400 nm. Light intensity is determined by calibrated PD300 and PD300IR photodiodes (Ophir Optics).

PL measurements: PbS and PbS-CdS QDs films are deposited on quartz substrates by dropcasting (OA-capped) or by using the aforementioned layer-by-layer technique (BDT-capped). The samples are then annealed at 140 °C for 5 minutes. The samples were excited at 400 nm by the second harmonic of a modelocked Ti:Sapphire (Mira 900) laser delivering pulses of 150 fs. An optical pulse selector is used to vary the repetition rate of the exciting pulse. Time-resolved traces are recorded with a Hamamatsu streak camera working in synchroscan mode and single sweep mode for different lifetime measurements. All measurements are performed in an optical cryostat. Samples are

loaded inside a glove box to maintain an oxygen-free environment at all times.

Impedance spectroscopy: Impedance spectroscopy measurements were conducted under dark conditions. A forward bias ranging from 0 - 0.8 V is superimposed with a 15 mV ac signal over the frequency range 1 MHz-50 mHz. The data are fitted using the equivalent circuit displayed in the inset of Figure 3.4 to extract the capacitance.

References

[1] K. Szendrei, W. Gomulya, M. Yarema, W. Heiss, M. A. Loi, *Appl. Phys. Lett.* **2010**, *97*, 203501.

[2] S. Tsang, H. Fu, R. Wang, J. Lu, K. Yu, Y. Tao, *Appl. Phys. Lett.* **2009**, *95*, 183505–1.

[3] N. Zhao, T. P. Osedach, L.-Y. Chang, S. M. Geyer, D. Wanger, M. T. Binda, A. C. Arango, M. G. Bawendi, V. Bulovic, *ACS Nano* **2010**, *4*, 3743.

[4] J. M. Luther, M. Law, M. C. Beard, Q. Song, M. O. Reese, R. J. Ellingson, A. J. Nozik, *Nano Lett.* **2008**, *8*, 3488.

[5] A. G. Pattantyus-Abraham, I. J. Kramer, A. R. Barkhouse, X. Wang, G. Konstantatos, R. Debnath, L. Levina, I. Raabe, M. K. Nazeeruddin, M. Grätzel, E. H. Sargent, *ACS Nano* **2010**, *4*, 3374.

[6] P. Maraghechi, A. J. Labelle, A. R. Kirmani, X. Lan, M. M. Adachi, S. M. Thon, S. Hoogland, A. Lee, Z. Ning, A. Fischer, A. Amassian, E. H. Sargent, *ACS Nano* **2013**, *7*, 6111.

[7] J. Tang, K. W. Kemp, S. Hoogland, K. S. Jeong, H. Liu, L. Levina, M. Furukawa, X. Wang, R. Debnath, D. Cha, K. W. Chou, A. Fischer, A. Amassian, J. B. Asbury, E. H. Sargent, *Nat. Mater.* **2011**, *10*, 765.

[8] S. Z. Bisri, C. Piliego, M. Yarema, W. Heiss, M. A. Loi, *Adv. Mater.* **2013**, *25*, 4309.

[9] K. Szendrei, M. Speirs, W. Gomulya, D. Jarzab, M. Manca, O. V. Mikhnenko, M. Yarema, B. J. Kooi, W. Heiss, M. A. Loi, *Adv. Funct. Mater.* **2012**, *22*, 1598.

[10] A. Rath, F. P. García de Arquer, A. Stavrinadis, T. Lasanta, M. Bernechea, S. L. Diedenhofen, G. Konstantatos, *Adv. Mater.* **2014**, *26*, 4741.

[11] W. Yoon, J. E. Boercker, M. P. Lumb, D. Placencia, E. E. Foos, J. G. Tischler, *Sci. Rep.* **2013**, *3*, doi:10.1038/srep02225.

[12] M. S. de la Fuente, R. S. Sánchez, V. González-Pedro, P. P. Boix, S. G. Mhaisalkar, M. E. Rincón, J. Bisquert, I. Mora-Seró, *J. Phys. Chem. Lett.* **2013**, *4*, 1519.

[13] L.-H. Lai, L. Protesescu, M. V. Kovalenko, M. A. Loi, *Phys. Chem. Chem. Phys* **2014**, *16*, 736.

[14] B. A. Gonfa, H. Zhao, J. Li, J. Qiu, M. Saidani, S. Zhang, R. Izquierdo, N. Wu, M. A. El Khakani, D. Ma, *Sol. Energ. Mater. Sol. C.* **2014**, *124*, 67.

[15] D. C. J. Neo, C. Cheng, S. D. Stranks, S. M. Fairclough, J. S. Kim, A. I. Kirkland, J. M. Smith, H. J. Snaith, H. E. Assender, A. A. Watt, *Chem. Mater.* **2014**, *26*, 4004.

[16] P. R. Brown, D. Kim, R. R. Lunt, N. Zhao, M. G. Bawendi, J. C. Grossman, V. Bulović, *ACS Nano* **2014**, *8*, 5863.

[17] S. Z. Bisri, E. Degoli, N. Spallanzani, G. Krishnan, B. J. Kooi, C. Ghica, M. Yarema, W. Heiss, O. Pulci, S. Ossicini, M. A. Loi, *Adv. Mater.* **2014**, *26*, 5639.

[18] M. Kovalenko, R. Schaller, D. Jarzab, M. Loi, D. Talapin, *J. Am. Chem. Soc* **2012**, *134*, 2457.

[19] I. Moreels, K. Lambert, D. Smeets, D. De Muynck, T. Nollet, J. Martins, F. Vanhaecke, A. Vantomme, C. Delerue, G. Allan, Z. Hens, *ACS Nano* **2009**, *3*, 3023.

[20] E. J. Klem, H. Shukla, S. Hinds, D. D. MacNeil, L. Levina, E. H. Sargent, *Appl. Phys. Lett.* **2008**, *92*, 212105.

[21] C. Piliego, L. Protesescu, S. Z. Bisri, M. V. Kovalenko, M. A. Loi, *Energy Environ. Sci.* **2013**, *6*, 3054.

[22] L.-H. Lai, W. Gomulya, L. Protesescu, M. V. Kovalenko, M. A. Loi, *Phys. Chem. Chem. Phys* **2014**, *16*, 7531–7537.

[23] F. Fabregat-Santiago, G. Garcia-Belmonte, I. Mora-Seró, J. Bisquert, *Phys. Chem. Chem. Phys* **2011**, *13*, 9083–9118.

[24] I. Kang, F. W. Wise, *J. Opt. Soc. Am. B* **1997**, *14*, 1632.

[25] R. S. Sanchez, E. Binetti, J. A. Torre, G. Garcia-Belmonte, M. Striccoli, I. Mora-Sero, *Nanoscale* **2014**, *6*, 8551–8555.

[26] B. L. Wehrenberg, C. Wang, P. Guyot-Sionnest, *J. Phys. Chem. B* **2002**, *106*, 10634.

[27] D. C. Lee, I. Robel, J. M. Pietryga, V. I. Klimov, *J. Am. Chem. Soc* **2010**, *132*, 9960.

[28] K. W. Kemp, A. J. Labelle, S. M. Thon, A. H. Ip, I. J. Kramer, S. Hoogland, E. H. Sargent, *Adv. Energy Mater.* **2013**, *3*, 917.

[29] S. M. Sze, K. K. Ng, *Physics of Semiconductor Devices*, Wiley, Hoboken, NJ, USA, **2007**.

[30] M. A. Hines, G. D. Scholes, *Adv. Mater.* **2003**, *15*, 1844–1849.

[31] M. V. Kovalenko, R. D. Schaller, D. Jarzab, M. A. Loi, D. V. Talapin, *J. Am. Chem. Soc* **2012**, *134*, 2457.

[32] J. M. Kroon, M. M. Wienk, W. J. H. Verhees, J. C. Hummelen, *Thin Solid Films* **2002**, *403*, 223.